Article

Improvement of Ultrasonic Inspection of the Forging Titanium Alloy

Teodor Tranca[1], Juliana Radu[2]

[1] AROEND -Romania; teodortranca@yahoo.com
[2] ZIROM-SA – Romania; iuliana.radu@zirom.ro
* Correspondence: teodortranca@yahoo.com; Tel.: +40723664051

Abstract:

Titanium's accelerating usage in global markets is attributable to its distinctive combination of physical and metallurgical properties. The key to best utilizing titanium is to exploit these characteristics, especially as they complement one another in a given application, rather than to just directly substitute titanium for another metal. Titanium alloy are extensively used in aerospace applications such as components in aero-engines and space shuttles, mainly due to their superior strength to weight ratio. For these demanding applications functionality and reliability of components are of great importance. To increase flight safety, higher sensitivity inspections are sought for rotating parts. Increased sensitivity can be applied at the billet stage, the forging stage, or both. Inspection of the forging geometry affords the opportunity to apply the highest sensitivity due to the shorter material paths when compared to those required for billet inspections. Forging inspection is typically performed for titanium (Ti) rotating parts with immersion inspection and fixed-focus, single-element transducers. Increased gain is required with depth because the ultrasonic beam attenuates with distance and diverges beyond the focus position that is placed near the surface. The higher gain that is applied with depth has the effect of increasing the UT noise with depth. The relationships between the UT noise, selection of the examination technique and the smallest detectable defect are presented in this material.

Keywords: Pulse Volume, Signal Noise Ratio, Automated Ultrasonic Testing, Simulation Software.

1. Introduction

This paper addresses the main two challenges of ultrasonic inspection of forged TI alloys: material's noise and the difficult correct evaluation of defects smaller than the wavelength of used soundwave.
For the first case we have proposed several methods to optimize the Pulse Volume within the area covered by the ultrasonic transducer, achieving a decrease of the Material's Noise and improving the Signal to Noise Ratio.
The second challenge appears when measuring defects comparable with the size of the ultrasonic wavelength and is described by the deviations of the measured results versus the theoretical calculations. For this case we have performed a qualitative analysis of the phenomenon by using the boundary element method (BEM).
The two topics have been analyzed by running the CIVA 11 Simulation Software. The output of these virtual tests has been analyzed in order to highlight the advantages and disadvantages of this method applied in the design of the test procedures. Another focus area was represented by the limitations of the current simulation software when used in the evaluation of the small defects combined with the effects of material's noise.

Preprints (www.preprints.org) | NOT PEER-REVIEWED | Posted: 9 May 2019 doi:10.20944/preprints201905.0111.v1

2. DAC Compensation

The ultrasonic inspection of the Titanium forgings billets is performed using Linear Testing or Helical Testing (see Figure 1). With Helical Testing, the billet is rotated while one or several probes, linear focused, are moved along its length. The billet is thus inspected along a helical path. The pitch during testing is adjustable between 1 and 15 mm per revolution, depending on parameters such as probe geometry, received signal to noise ratio, billet surface condition, internal grain structure, desired quality class, etc.

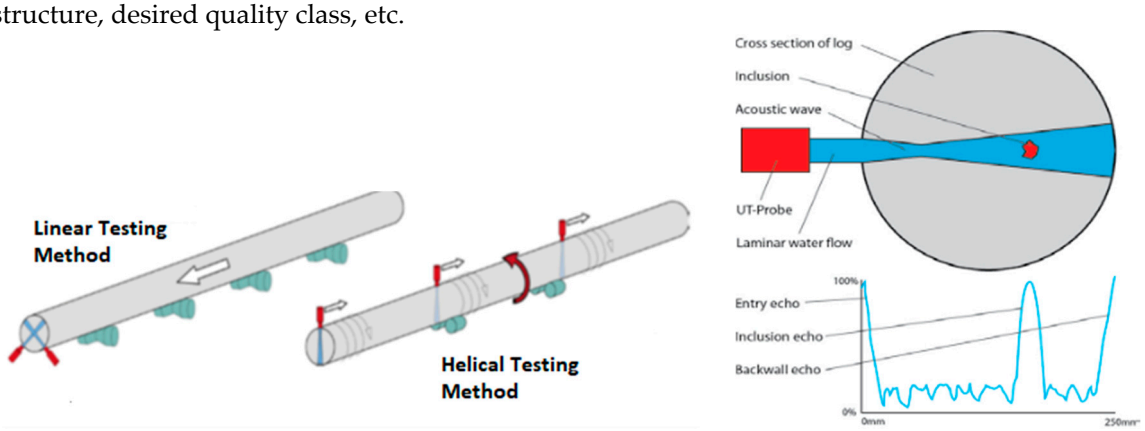

Figure 1-Automated Ultrasonic Testing of the Billets

Calibration billets provided with flat bottom holes are used for the calibration of the probes. The billet volume is scanned by probes arranged perpendicular to the billet. The entry echo is monitored as a function check and the back-wall echo as well as any echo from a defect are continuously recorded as amplitude and delay time.

Electronic Distance Amplitude Correction - DAC (Figure 2) is applied in order to equalize the signal's amplitude of the reflector, regardless of its distance from the source. Increased gain is required by the additional depth because the ultrasonic (UT) beam attenuates with distance and diverges beyond the focus position that is placed near the surface. The level of the noise becomes inacceptable because the gain that is applied as the effect of amplifying the UT noise, especially when the thickness of the material exceeds 50 mm. In such cases, a second zone inspection is applied, where the transducer beam focus is moved further into the part, either by moving the transducer closer to the surface or using a different transducer that has different focusing characteristics. Afterwards a second scan is made with an inspection gate on the deeper region.

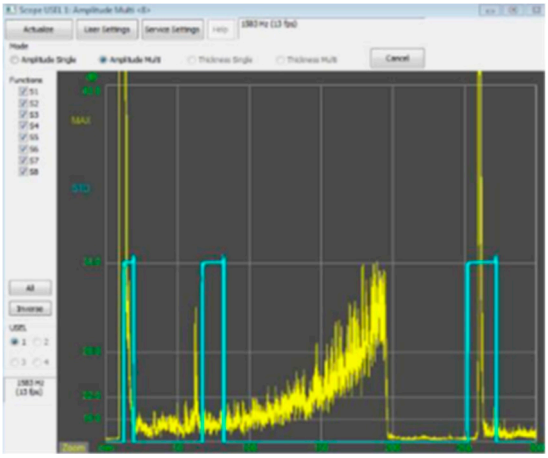

Figure 2 -Distance Amplitude Correction

Preprints (www.preprints.org) | NOT PEER-REVIEWED | Posted: 9 May 2019 doi:10.20944/preprints201905.0111.v1

3. Ultrasonic Grain Noise

The grain noise appears during the ultrasonic inspections of the forgings product and has a strong effect to decrease the amplitude of the echoes caused by small or subtle defects detected in the material. Generally, "grain noise" is related to the root mean square signal (RMS) determined by the microstructure of the examined metal.

An ultrasonic wave propagating in a polycrystalline medium composed of randomly oriented anisotropic grains will lose energy to scattering at the grain boundary interfaces. Scattering is observed if difference regarding the stiffness properties exists between the grains (Figure 3).

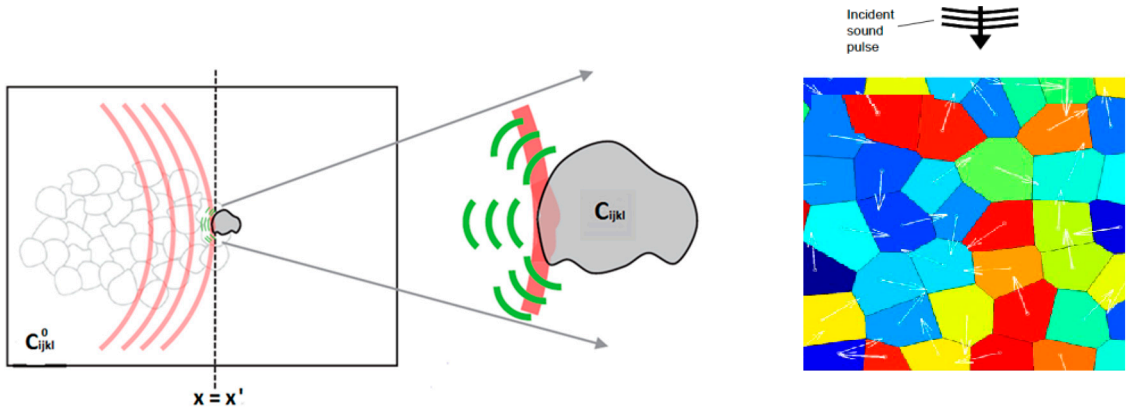

Figure 3. A wave is shown to have propagated through a statistically adequate number of grains such that C^0 ijkl defines its phase velocity. A grain with elasticity Cijkl located at x′ scatters a fraction of the waves energy because Cijkl ≠ C^0 ijkl [1]

From metallographic point of view, the scattering can be related to the dimension of the grain, the shape (elongation), the stress, and texture.

The forgings products made from Ti6-4 present many structures having different length of scales;

- At the first level of the scale are the individual micro grains, i.e., composed by a single crystal with the atoms disposed in a regular lattice (see Figure 4a).
- Many micro grains have the possibility to colonize and form large entities as platelets or macro grains reaching a dimension comparable with the wave length of the incident sonic radiation (see Figure 4b).
- Somme structures, as macro grains, become large enough to be observed without optical aids, especially after the properly machining of the metallic surface (etched), as shown in Figure 4c.

a. 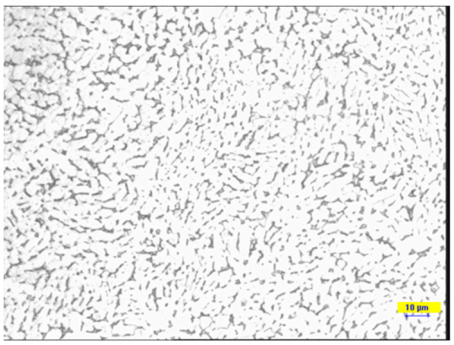

b. 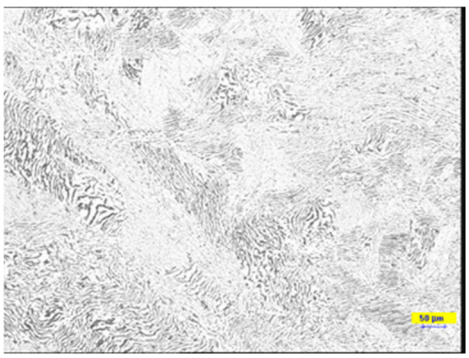

Preprints (www.preprints.org) | NOT PEER-REVIEWED | Posted: 9 May 2019 doi:10.20944/preprints201905.0111.v1

c. 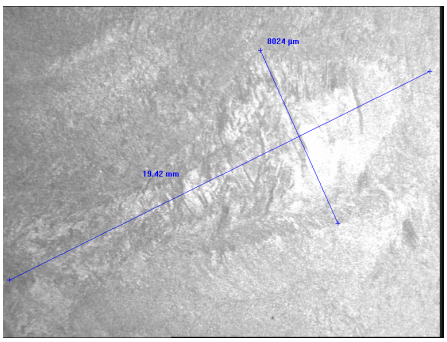

Figure 4. Different degree of grains colonization

The anisotropic stiffness properties of crystallites cause the material to be heterogeneous, which forms the underlying cause for scattering. Namely, two neighboring grains which have different orientations, create a difference in wave velocity (an acoustic impedance mismatch) at their boundary. Consequently, an incident wave upon this interface causes a scattering event to occur, the strength of which is determined by the intensity of the impedance contrast. Hence the scattering strength of a material is in part determined by the maximum possible difference in stiffness which can occur through two orthogonal orientations.

The adverse effects of scattering can be summarized by discussing an increased attenuation, the introduction of coherent noise and possibly anisotropic effects.

The general appearance of grain noise during an UT inspection is illustrated in Figure 5. Consider a UT A-scan depicting received signal amplitude versus arrival time for a fixed transducer location above a forging. As shown in the Figure 5, grain noise appears as a complex hash following the front-wall echo. Most forging inspections make use of one or more time gates (depth zones), like that depicted in red.

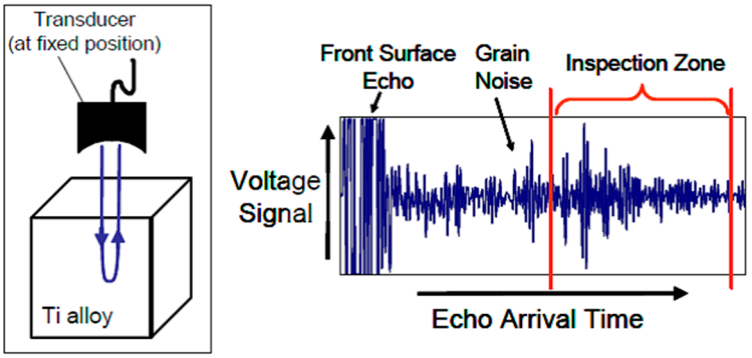

Figure 5. Typical Appearance of UT Grain Noise in A-Scan

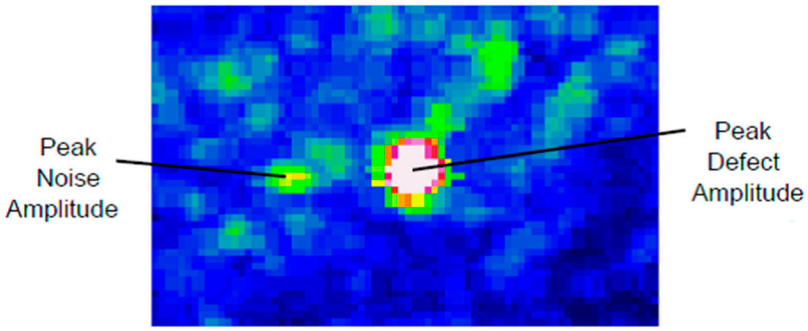

Figure 6. UT „C"- Scan Containing an FBH Indication in the Presence of Noise [2]

Preprints (www.preprints.org) | NOT PEER-REVIEWED | Posted: 9 May 2019 doi:10.20944/preprints201905.0111.v1

The ability of the system to distinguish signals from noise (usually quantified by the Signal-to-Noise Ratio) is severely reduced by the presence of the grain noise.
The spatial correlation of backscattered ultrasonic grain noise has important implications in practical ultrasonic inspections. For example, the C-scan image (see Figure 6) constructed by using the gated-peak signals (containing both flaw and noise signal) is the routine output in most industrial ultrasonic testing operations.
Figure 7 presents a "B" scan made by an automated ultrasonic system (AUT) on a cylindrical reference block supplied with two artificial reflectors (Φ1.2 mm FBH and Φ2.0 mm FBH). The grain noise is visible in the diagram representing the record of the control and is related to the transducer's frequency and the position of the defect into the reference block.

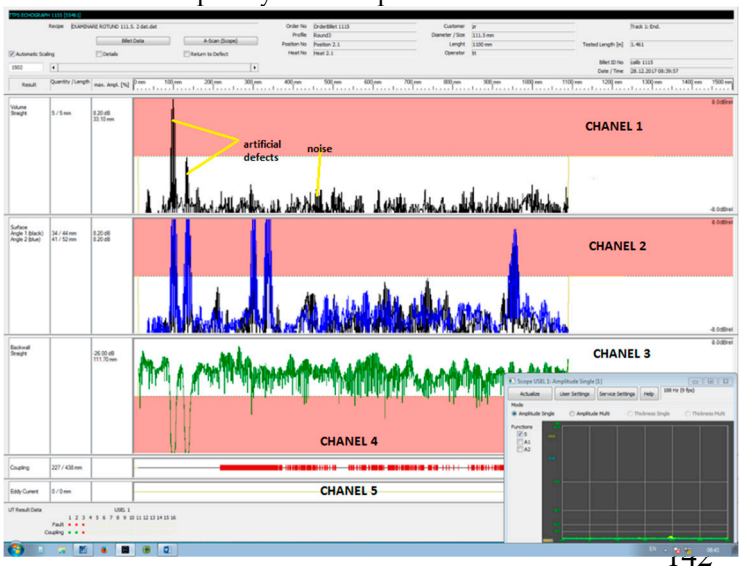

CHANNEL 1: Control with normal transducer (S)
CHANNEL 2: Control with 2 angled transducers (A1 and A2)
CHANNEL 3: Monitoring of the back wall echo
CHANNEL 4: Monitoring of the ultrasonic coupling
CHANNEL 5: Control with Eddy Current

Figure 7. UT „B"- Scan containing Indications of Defects and Grain Noise

3. Signal-to-Noise Ratio

Signal-to-Noise Ratio (SNR) is a measure of the grain noise severity. Two of the more common definitions are: (1) the simple ratio of the peak amplitudes of the reference signal and the noise and (2) same terms with the average noise background subtracted, so that the numerator and denominator each describe how much the respective peak amplitude exceeds the average background level.

$$\frac{S}{N} = \frac{\text{peak defect amplitude}}{\text{peak noise amplitude}} \quad (1)$$

$$\frac{S}{N} = \frac{\text{peak defect} - \text{avg.noise}}{\text{peak noise} - \text{avg.noise}} \quad (2)$$

It is very dificult to detect a defect by examining a C-scan if its SNR is too low, e.g., near or below unity and the defect is small in lateral extent. During the inspection protocol, it is recomended to ensure an adequate SNR for critical defects expected to be reveled.
One of the first challenges to study backscatter was to find a means to quantify it. The Figure-of-Merit (FOM) was introduced to this end which succeeded in experimentally measuring the inherent noise severity of a sample, independent of the inspection configuration used. This FOM is related to the time-domain RMS noise *Nrms* observed in an A-scan. The absolute noise Ievel or S/N ratio is approximately proportional to the FOM value at the center frequency. For example, having a fix

Preprints (www.preprints.org) | NOT PEER-REVIEWED | Posted: 9 May 2019 doi:10.20944/preprints201905.0111.v1

configuration of examination, a material having a FOM of 2 produces an noise having a level double than an material having a FOM of unity.

$$Nrms \sim FOMC_1 \iiint_{-\infty}^{\infty} C^4(x,y,z)\, dxdydz \quad (3)$$

Where:
- C_1 represents the variables associated with the inspection configuration,
- The volume integral of C represents the incident beam

Equation (4) shows the definition of FOM, where n is the number of scatters, $Arms$ is an average of their scattering amplitude. [3]

$$FOM = \sqrt{n}\ Arms \quad (4)$$

The frequency dependent backscatter for a cubic material, and its relation with FOM, is shown in equation (5):

$$\eta(\omega) = FOM(\omega^2) = \left(\frac{\omega^2}{4\pi\rho C_L^4}\right)^2 \langle \delta 4 C_{33}^2 \rangle \left[\frac{8\pi A_g^3}{\left(1+(2kA_g)^2\right)^2}\right] \quad (5)$$

$$\langle \delta C_{33}^2 \rangle = \frac{16(c_{11}^2 - 2c_{11}\, c_{12} + c_{12}^2 - 4c_{11}c_{44} + 4c_{12}c_{44} + 4c_{44}^2)}{525}$$

Where:

Ag - a correlation distance equal to half of the effective linear dimensions of the grain,
ω - the angular frequency,
k - the wave vector.

The frequency-dependent FOM must be known if absolute noise predictions are to be made using these models. The multi-phase microstructures of titanium alloys are quite complex, and tend to vary with position in billets and forgings. It is unlikely that measurements of noise, Figures-of-Merit will become a routine part of industrial inspections in the near future. In this paper we will make such predictions of the dependence of noise on transducer choice, sonic pulse volume, gate choice and entry surface curvature. [4]

4. Dependence of Grain Noise on the Volume of the Ultrasonic Pulse

It is important to study the relationship between backscattered noise and the volume of the incident sonic pulse (figure 8a). The pulse volume was determined by measuring the time duration of a back-wall echo (see Figure 9) and the lateral area of the focal spot. The spot size was determined by scanning into the reference blocks a 1.2 mm FBH (see Figure 10) and analyzing the resulting scan image (see Figure 11). Backscattered gated-peak grain noise was then measured using a gate centered at the focal plane. If the pulse hits a reflector, the sonic energy will be reflected towards the transducer from the reflector itself and also from the metal grains surrounding it. To avoid the reflection from the grains, it is desirable that the cross area of the pulse volume in the region of the defect to encompass the defect and a smallest number of grains.
In this case, to increase the SNR, the pulse volume should decrease, because:

Preprints (www.preprints.org) | NOT PEER-REVIEWED | Posted: 9 May 2019 doi:10.20944/preprints201905.0111.v1

a. the reflectivity of a given grain compared to that of the embedded reflector is relatively independent of the pulse volume if both are hit by the pulse and,
b. if the pulse volume is reduced, a small number of grains are excited, which can produce echoes arriving at the same time as the echo from the reflector (Figure 8b).

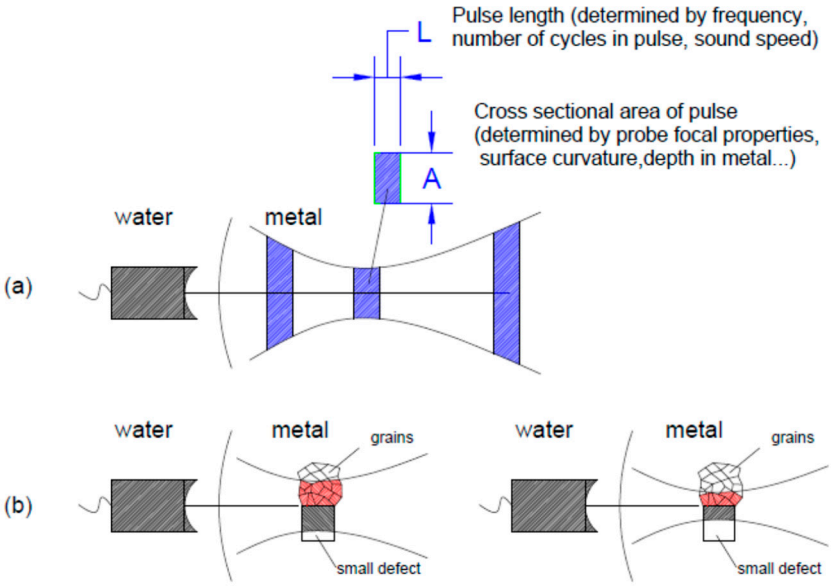

Figure 8. (a) The Volume of the Sonic Pulse is related to the position on the beam axis, (b) If the amount of reflected energy due to the Grains positioned around the Defect is small, SNR is increasing.

The Experimental way to determine the Pulse Volume in the focal area of the ultrasonic transducer is the following:
(1) Using RF presentation, we measure the back–wall echo duration and transform that into a pulse length (see Figure 9).

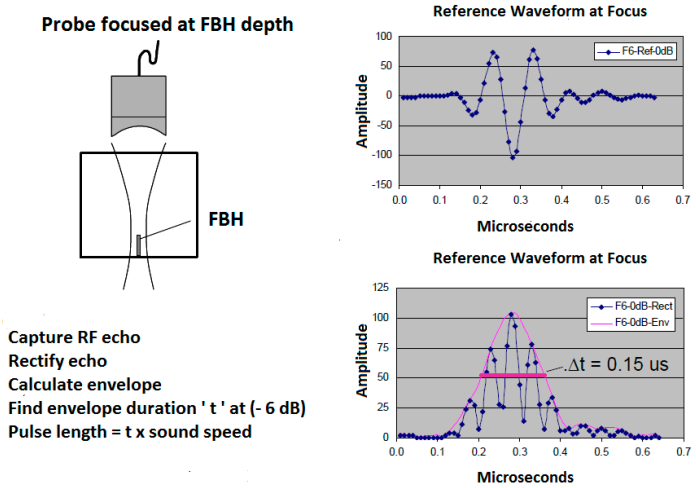

Figure 9. Determination of Sonic Pulse Length for the Transducer Focused at the FBH Depth [5]

Preprints (www.preprints.org) | NOT PEER-REVIEWED | Posted: 9 May 2019 doi:10.20944/preprints201905.0111.v1

(2) Using the reference block, the lateral area of the pulse in the focal zone is measured. That was done by scanning in both directions (axial and rotation) the focal area of the transducer over a FBH placed in the reference block (see Figure 10).

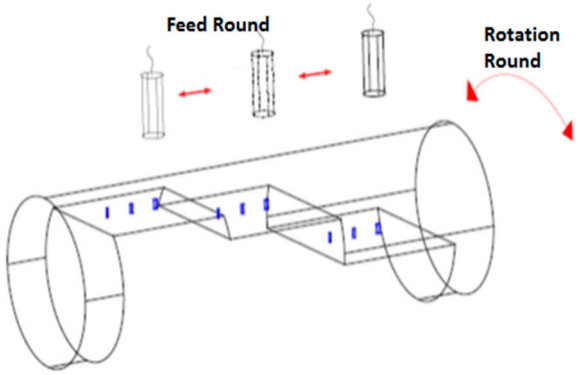

Figure 10. Determination of the lateral extensions using the Reference Block

In order to realize these determinations, a focused 5 MHz transducer, with 20 mm crystal diameter and 200 mm water focal distance immersion transducer was used. The lateral extensions were determined by scanning the transducer having many 1.2 mm FBH, disposed at increasing depths into material. It is important to achieve the determination in real examination conditions, respectively in circular direction and feed directions (see Figure 10). The values of the lateral extensions determined, are shown in Figure 11.

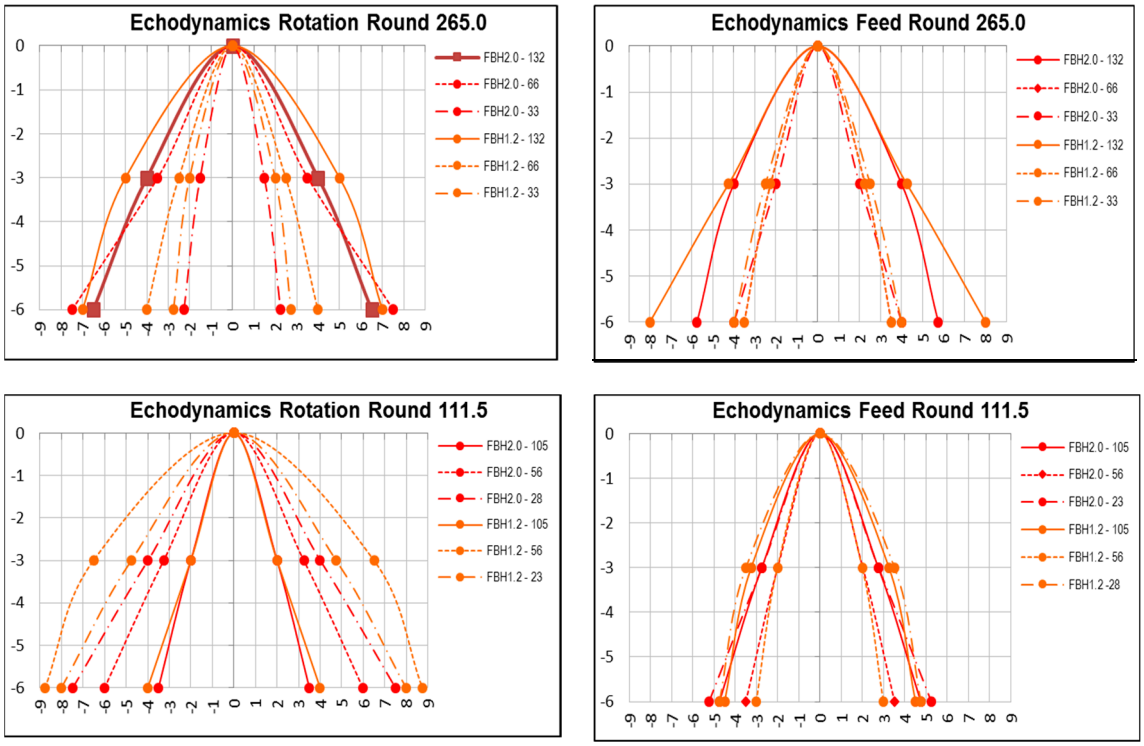

Figure 11. Graphics presenting the values of the lateral extensions

The curvature of the entry affects the ultrasonic beam shape inside the material (see Figure 12). The amplitude of defect echoes and the level of competing grain noise are affected as well.

Preprints (www.preprints.org) | NOT PEER-REVIEWED | Posted: 9 May 2019 doi:10.20944/preprints201905.0111.v1

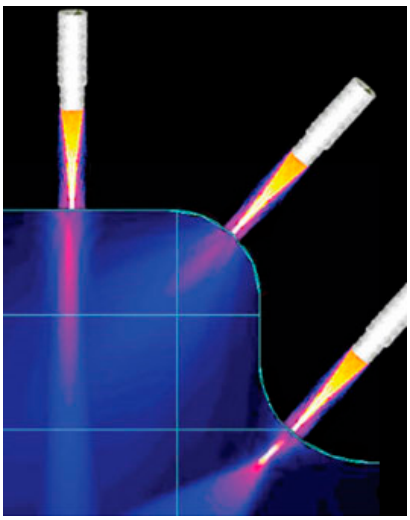

Figure 12. The modification of the focal distance in material related to the curvature of the surface

The difference in diameter leads to significant changes of the examination settings although the same transducer is used for each measurement, positioned at fix water path (90 mm) and the materials of the two blocks have the same (identical) chemical composition, heat treatment and ultrasonic transparency. Both the Lateral Extension and the Gain Correction Curve (see Figure 13) are strongly affected by the value of the billet radius.

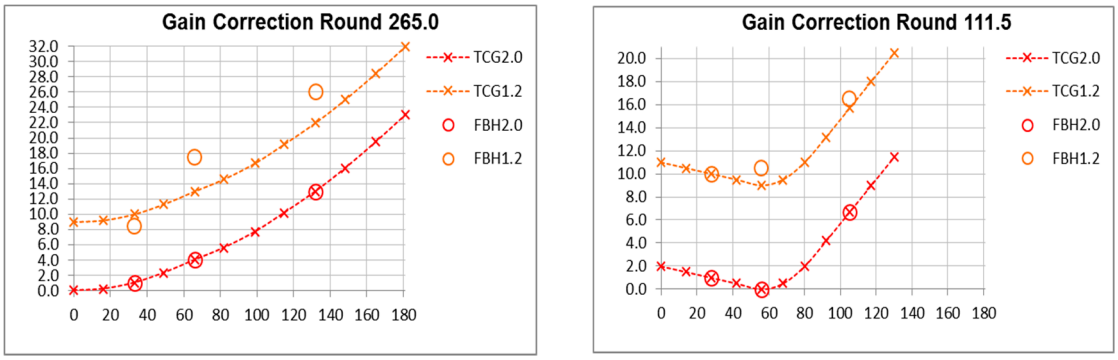

Figure 13. The influence of the Billet Radius over the Gain Correction Curve

5. Relationship between SNR and the Pulse Volume

The Rule of Thumb represents a mathematical expression established empirically between SNR and the Pulse volume. [6]
This Rule establishes the report between SNR and 1/ the square root of the sonic pulse, for a fixed frequency and at the depth of the flaw. The noisiness of the microstructure is a constant of proportionality (so-called Figure of Merit) and the reflectivity of the defect, as quantified by the scattering amplitude A flaw. The noisiness of the microstructure is determinant for the value of the SNR. The rule is applied in conditions of the signal to noise computed using the peak (on axis) defect amplitude and the average grain noise level (RMS).
Considering the case of a small flaw located along the beam's axis (but not necessarily in the focal area) and using the approximations of "Gaussian Beam" and "tone-burst", the ratio of flaw signal amplitude to " RMS" grain noise" is givens by equation (6):

Preprints (www.preprints.org) | NOT PEER-REVIEWED | Posted: 9 May 2019 doi:10.20944/preprints201905.0111.v1

$$\text{SNR} \propto \left[\frac{Aflaw(\omega)}{\sqrt{\eta(\omega)}}\right]\frac{1}{\sqrt{B^2\Delta tp}} \quad (6)$$

Where:

B - the average beam diameter,

Δtp - the sonic pulse length or the product of velocity and pulse time length,

$Aflaw$ - the far field scattering amplitude of the defect.

The equation (6) also predicts the SNR to change according to the change in ratio between A *flaw* and FOM with frequency. This determines the introduction of multi-zone transducers a configuration of transducers which each focus at a different depth within the billet, to improve overall SNR.

The whole billet volume is zoned into several inspection zones with different depths, as shown in Figure 14. The inspection zones are determined by the focal zone parameters of the transducers, the formulas used for the calculation of the –6 dB depth of field and the –6 dB beam diameter are the following:

$$L = L_{-6dB} \approx 4\lambda \left(\frac{F}{D}\right)^2 \quad (7)$$

$$\phi = \phi_{-6dB} \approx 1.03\lambda \frac{F}{D}$$

Where:

L is the –6 dB depth of field,

ϕ is the –6 dB beam diameter,

F is the focal length,

D is the transducer diameter,

λ is the wavelength.

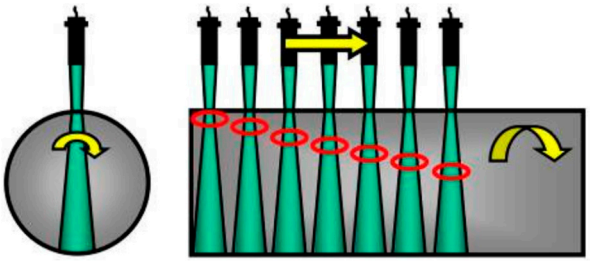

Figure 14. Helical multi-zone testing with many focused probes [7]

6. The Inspection Improvement

We propose to analyze two different diameters references blocks scanned on the AUT system. The diagrams from Figure 11 and Figure 13 present the main ultrasonic characteristics of the blocks. For each examination, the gain of the system was set so that the response from the Φ 1.2 mm FBH reference hole would be at 60% , respectively 50% full screen height (FSH). In these conditions, the peak noise amplitude at the depth of the FBH was measured. It is visible in the B-scan (Figure15 and Figure 16) that the FBH are essentially equal, but the noise levels are higher for the weaker focusing transducer. This is a demonstration of the improvement in SNR that occurs when the pulse volume is lower.

Because the ultrasonic equipment was identical in both situations (same line-focused transducer, positioned at same water path) the focusing will be different because of the difference in curvature of the entry surfaces of the billets. That is highlighted in Figure 11 where are presented the lateral extensions of the sound beam for each testing block (respectively Ø 111.5 and Ø 265.0 mm).

Preprints (www.preprints.org) | NOT PEER-REVIEWED | Posted: 9 May 2019 doi:10.20944/preprints201905.0111.v1

As a result of the influence of the entry surface, the pulse volume will be lower in the examination of Ø265.0 block and higher for the Ø111.5 block.

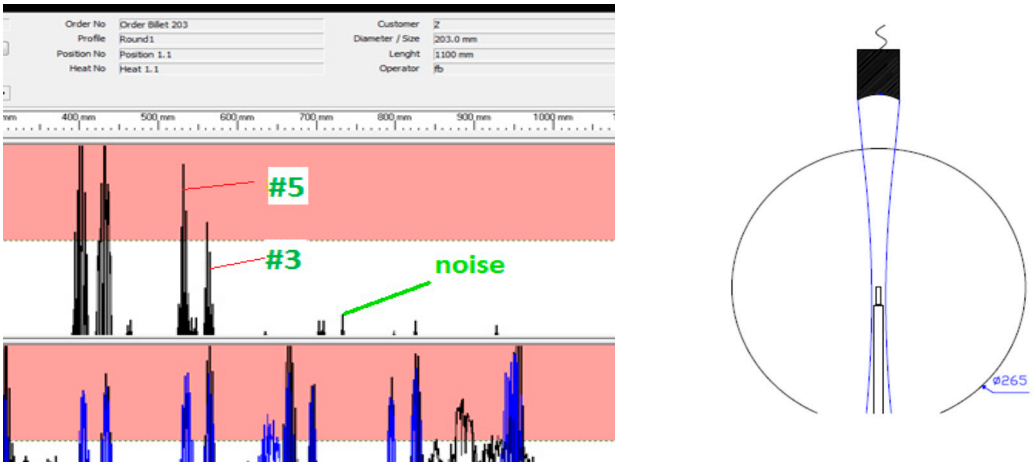

Figure15. The focal plane located at the FBH depth; Φ 1.2 mm FBH at 60% FSH (Φ 2.0 mm FBH at 130% FSH). Peak noise amplitude at 12% of screen height; SNR ~5:1

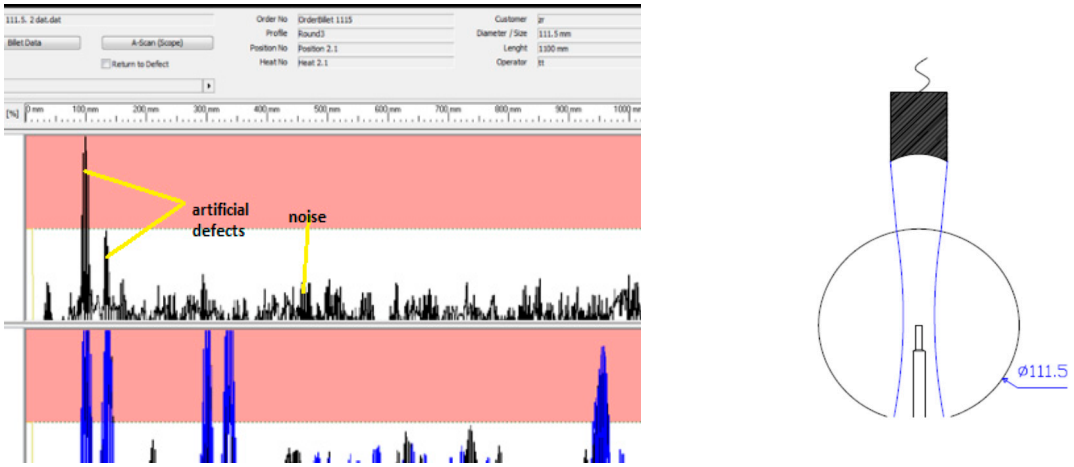

Figure 16. FBH located beyond the focal plane. Φ1.2 mm FBH at 50% FSH (Φ2.0 mm FBH at 130%FSH). Peak noise amplitude at 25% of screen height; SNR ~2

7. Correct dimensioning of the reflectors smaller than one wavelength

The necessity to detect and size smaller defects is higher depending on the material's technology and ultrasonic inspection of the Titanium forgings. Measurement of ultrasonic indication is generally performed by echo dynamic (area amplitude based sizing). Echo dynamic sizing (sizing by probe travel, e.g. -6 dB drop method) are used for discontinuities larger than the beam spread and area-amplitude based sizing procedures are applied (like DAC or DGS)for indications smaller than the beam spread.

Area-amplitude based sizing procedures compare the reflection of an indication to the reflection of reflectors with known dimension, e.g. artificial reflectors like flat bottom holes (FBH) or side drilled holes (SDH). One of the most traditional procedures used from the first days of the ultrasound testing is the Distance Amplitude Correction (DAC), that is based on calibration managing multiple

Preprints (www.preprints.org) | NOT PEER-REVIEWED | Posted: 9 May 2019 doi:10.20944/preprints201905.0111.v1

flat bottom holes machined into calibration blocks and some extrapolation based on the inverse square law.

7.1. Disagreement with area-amplitude relationship

The area-amplitude relationship is a consequence of using the Kirchhoff approximation (also called physical optics) when solving the equations governing ultrasound scattering by an FBH. This approximation assumes that the motion of the FBH surface when reflecting an ultrasound pulse is identical to the motion that would occur if the pulse would be reflecting from an infinite planar surface. A further assumption in obtaining the area-amplitude relationship is that the finite width ultrasound beam can be approximated as an infinite plane wave. Under these assumptions, it is seen that the FBH surface motion will be independent of the size of the FBH. Auld's reciprocity formula [8] states that the voltage received from a void defect is the integral over the defect surface of the product of the traction generated by the incident pulse in the absence of the defect, multiplying the total surface motion of the defect in response to the incident pulse. In the case of the FBH using the Kirchhoff approximation with an incident plane wave, it is readily seen that Auld's formula predicts an output voltage in direct proportion to the area of the FBH, i.e., the area amplitude relationship.

The relationship between echo response and FBHs has been addressed since some of the earliest developments in ultrasonic testing. Krautkramer [9] referred to these as a disk shaped reflector (DSR) and developed the famous AVG (English DGS) method of relating amplitude responses from FBHs to curves made for each style of probe. The relationship between echo amplitude and probe and FBH size can be summarised in the form of an equation.

$$\frac{V_f}{V_0} = \frac{SA}{\lambda^2}\frac{1}{T^2}e^{-2T\delta} \quad (8)$$

Where:

V_f = the maximum amplitude of the echo from the target

V_0 = the maximum possible signal amplitude if all energy is returned to the receiver

T = the distance along the beam axis to the target

A = the area of the defect

S = the area of the probe

λ = the wavelength of ultrasound (nominal)

δ = the attenuation coefficient

Due to the findings of Krautkramer [9] it became possible to note that the amplitude change for a FBH was directly proportional to its area. Therefore, having set a response on the CRT to a specific amplitude (within the linear region of the instrument display) the response from a FBH half the area would produce a signal with half the amplitude and the response from a FBH double the area would produce a signal with double the amplitude.

As part of producing setup standards, a study was performed to determine if smaller FBH could be used by applying the theoretical gain difference in dB based on the area amplitude relationship. There are advantages to using biger FBHs since they can be drilled deeper and provide separation

Preprints (www.preprints.org) | NOT PEER-REVIEWED | Posted: 9 May 2019 doi:10.20944/preprints201905.0111.v1

between the back-wall signal and the signal from the bottom of the hole. The results of the UT measurements, however, indicated that a smaller difference was consistently observed rather than theortical dB difference (see Fig. 17). The cause of the discrepancy was determined by modeling the interaction of the beam produced by the specific transducers used and the FBHs. It was shown that interaction between the surface wave that is generated on the FBHs and the incident compression wave can have a constructive interference that raises the amplitude of the smaller FBH.

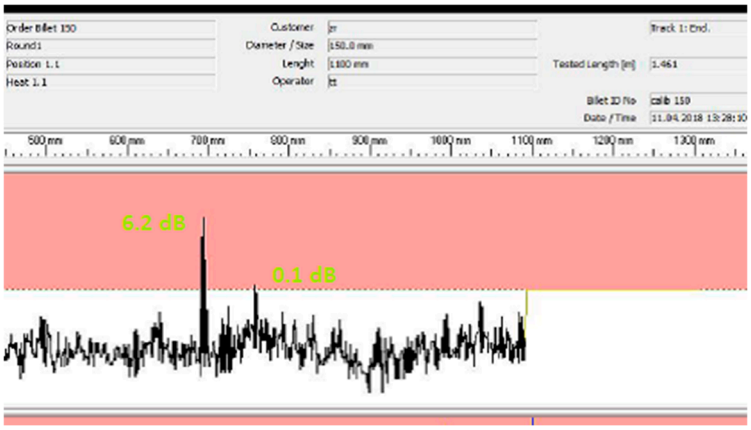

Figure 17. The difference between the signals of Φ 1.2 mm FBH and Φ 0.8 mm FBH is only 6.1 dB instead of 7.04 dB, the theoretical value (Φ 150.0 mm reference block).

A phenomenon that the classic theory fails to predict is the generation of diffracted waves at the corners of the FBH. Figure 18 depicts the various diffraction phenomena that occur for a plane compressional wave at perpendicular incidence on the FBH. It is seen that in addition to a reflected compressional wave, diffracted compressional and shear waves are generated, along with surface waves that propagate both down the bore of the FBH and across the top. Attention is directed to the surface waves propagating across the top of the FBH. Upon reaching the opposing corner of the FBH surface, the surface wave undergoes a second diffraction, during which a small amplitude diffracted compressional wave emerges from the FBH corner. Part of this secondary diffracted wave travels up to the transducer, slightly behind the primary compressional wave reflection from the FBH surface, as depicted in Figure 19, and is received as a small signal trailing the main reflection, as depicted in Figure 20. The time delay between these two waves is given by the product of the FBH diameter and the surface wave velocity.

If the time delay between these two signals is sufficiently small, an interaction could take place that would enhance or reduce the total signal amplitude through a constructive or destructive interference. Such an interaction might be the underlying cause of the deviation from the area-amplitude relation seen in experiments when looking at small reflectors.

Preprints (www.preprints.org) | NOT PEER-REVIEWED | Posted: 9 May 2019 doi:10.20944/preprints201905.0111.v1

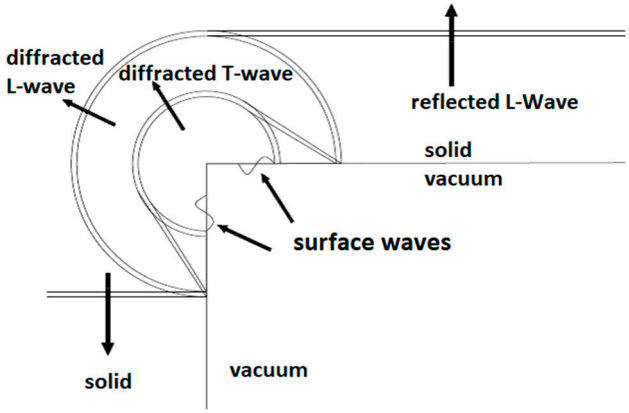

379

380 **Figure 18**- Wave Modes Generated When a Compressional L-Wave is Incident on an FBH [5]

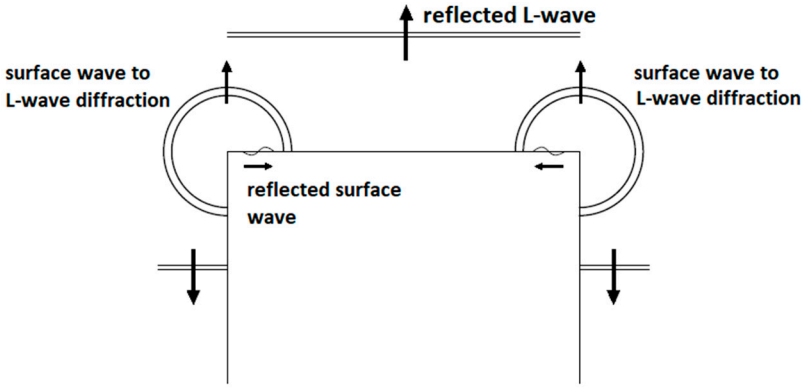

381

382 **Figure 19-** Refracted L-Wave Following the Reflected L-Wave [5]

383

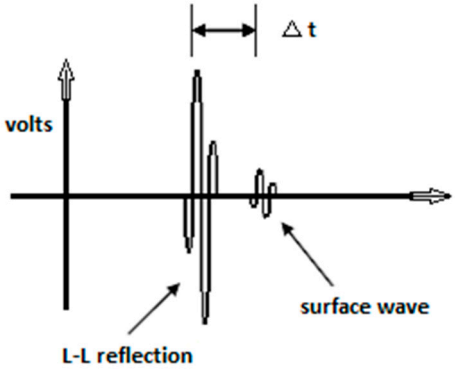

384

385 **Figure 20** - Two Signals Returned to the Transducer [5]

386 The challenge in determining the significance of the surface wave interaction is quantitatively
387 determining the amplitudes of the diffracted signals. For this purpose, a computer model was
388 employed that used a boundary element method (BEM) formulation to solve the equations
389 governing the surface wave diffraction phenomena on the FBH. The boundary element formulation
390 uses a high-frequency computational ansatz based on an asymptotic analysis of the diffraction
391 problem. Rather than using the asymptotic solution outright, this method uses the asymptotic result
392 as a starting point, then seeks to find corrections to the asymptotic solution to obtain an exact
393 numerical solution. The boundary elements are, therefore, used to compute corrections to the

Preprints (www.preprints.org) | NOT PEER-REVIEWED | Posted: 9 May 2019 doi:10.20944/preprints201905.0111.v1

asymptotic solution, rather than represent the entire solution. Consequently, extremely large problems can be treated with practical computational efficiency. Boundary elements are prescribed over the top and sides of the FBH. The FBH is assumed infinitely long and the medium is prescribed to have a small ultrasonic attenuation, so that the wave field effectively decays to zero after some distance along the FBH. This attenuation is made just small enough so that its presence is not noticed in the computed transducer response signals.

Using the boundary element formulation, the surface motions are computed on the FBH for a very high frequency, very broadband plane wave. The signals from one such computation can be used to predict the response for any signal with a center frequency within the bandpass of the computation, or equivalently, for any size FBH for an incident pulse of a given frequency, through appropriate filtering and scaling.

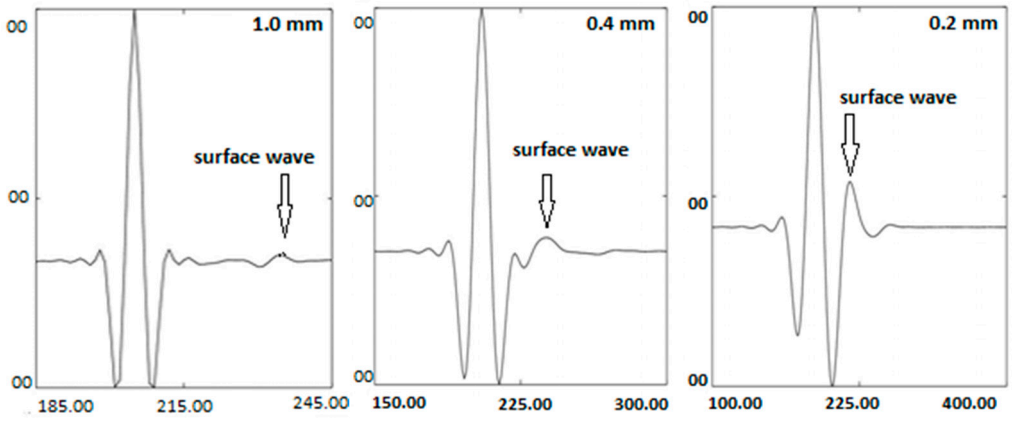

Figure 21 – Interaction of the Diffracted Surface Wave and the Reflected L-Wave for Three FBH Sizes [5]

Figure 21 compares signals for Φ 1.0 mm, Φ 0.4 mm, and Φ 0.2 mm FBHs. It is observed that the time delay between the two received signal components decreases as the hole becomes smaller. In the case of the Φ 0.2 mm FBH, the two signals are overlapping. The interaction between the two signals will depend on signal bandwidth: the narrower the bandwidth, the more significant the interaction.

8. Simulation software for NDT

The modern Non-Destructive Testing modelling is useful to assessing the detection capability and to elaborate the procedures for inspections. CIVA, developed by French CEA, is the commercially most successfully software in simulation of NDT situations. The program can handle different materials, geometries, cladding and anisotropy in arbitrary symmetry and orientation. Even simulation of material structures, different probe types and defects with arbitrary shape, size and orientation can be simulate.

Parameter studies can be used for review of important parameters, in order to find out limit values as well as which parameters are most important for the inspection system. In addition, optimization of defect content for the manufacture of test reference blocks can be done (see Table 2 and Table 3).

8.1. Principle of the Kirchhoff & GTD model

In the simulation used for ultrasonic examination of the planar defects, two classical scattering models have been used: Kirchhoff approximation, to simulate the reflection, and Geometrical Theory of Diffraction, to simulate the diffraction. Recently, it was developed, from the combination of these two theories, the Physical Theory of Diffraction (PTD) that retain the advantages of both. Every one of the classical ultrasonic inspection methods, (pulse echo, tandem or Time of Flight

Preprints (www.preprints.org) | NOT PEER-REVIEWED | Posted: 9 May 2019 doi:10.20944/preprints201905.0111.v1

Diffraction) perform the detection of the planar defects by interpreting their specular or diffraction echoes.

It is assumed that the Kirchhoff scattered field can be decomposed in an approximate manner in two parts: a geometrical field which includes the specular reflected field and a contribution arising from the flaw edge corresponding to the edge's diffraction field. The contribution of this diffraction field at the observation point x is characterized by same form as the GTD field but a different edge diffraction coefficient (depending on the α incidence and β observation directions and polarizations):

$$\boldsymbol{U^{KA(Diff)}(x) = D^{KA}_{\alpha\beta}(x)\frac{e^{ikr}}{\sqrt{kr}}} \quad (9)$$

It is noted that this coefficient defines the directivity of edge diffraction contribution according to the Kirchhoff approximation.

The physical theory of diffraction (PTD) consists in correcting the Kirchhoff edge diffraction field by that modelled by GTD.

This correction leads to add a corrective term to the KA scattered field (without far-field approximation). This corrective term is the difference of wave amplitudes diffracted by the edge, by GTD and KA.

$$\boldsymbol{U^{PTD}(x) = U^{KA}(x) + \left[D^{GTD}_{\alpha\beta}(x) - D^{KA}_{\alpha\beta}(x)\right]\frac{e^{ikr}}{\sqrt{kr}}} \quad (10)$$

The PTD field is the sum of the Kirchhoff field and a GTD modified field in which the GTD coefficient has been replaced by the difference between GTD and Kirchhoff edge diffraction coefficients. At the specular observation direction, the Kirchhoff field (without far-field approximation) is finite leading to an effective prediction of specular reflection. But the KA diffraction coefficient KA, $\boldsymbol{D^{KA}_{\alpha\beta}(x)}$ for edge diffraction contribution (previously obtained from a far field approximation of the Kirchhoff field) diverges and has the same singularity as the GTD edge diffraction coefficient GTD, $\boldsymbol{D^{GTD}_{\alpha\beta}}$(x). When making the difference of the two coefficients, their singularities cancel each other and the diffraction coefficients difference $\boldsymbol{D^{GTD}_{\alpha\beta}}$(x) -$\boldsymbol{D^{KA}_{\alpha\beta}(x)}$ is finite.

$$\boldsymbol{U^{PTD}(x) \approx U^{KA}(x)} \quad (11)$$

When the observation direction is far from to the specular direction, edge diffraction effects are predominant compared to reflection phenomena, the Kirchhoff field is equal to the Kirchhoff edge diffraction contribution and so cancels it so that the Kirchhoff & GTD model leads to similar results than the GTD model.

$$\boldsymbol{U^{KA}(x) \approx D^{KA}_{\alpha\beta}(x)\frac{e^{ikr}}{\sqrt{kr}}} \text{ and } \boldsymbol{U^{PTD}(x) \approx D^{GTD}_{\alpha\beta}(x)\frac{e^{ikr}}{\sqrt{kr}} = U^{GTD}(x)} \quad (12)$$

Flaws which can be modelled thanks to Kirchhoff & GTD are the same than with the GTD model: planar flaws (rectangular, semi-elliptical or CAD contour planar flaws), multi-facetted flaw and branched flaw. [10]

8.2. Model capability to be assessed

The model verification activities are divided into five different partial phases. Each phase is divided into a number of different tasks with specific purposes (see Table 1).

Preprints (www.preprints.org) | NOT PEER-REVIEWED | Posted: 9 May 2019 doi:10.20944/preprints201905.0111.v1

Table 1. Phases of the verification activities

Phase 1	Response prediction for simple/smooth defects in simple materials and probe modeling
Phase 2	Geometry handling with model
Phase 3	Complex materials – austenitic welds, inconels, dissimilar metal welds
Phase 4	Rough defects in simple materials
Phase 5	Rough defects in complex materials

The difference between simple/smooth defects and rough defects stated in Table 1 is that simple/smooth defects are typically artificial defects or an ideal fatigue crack. Rough defects are the type of defects that are typically service induced, with a clear morphology, following grain structure or other irregularities. By simple materials we understand the carbon steel or stainless parent material that shows isotropic behavior. Complex materials, like Titanium alloys, show anisotropic behavior with significant influence on the sound beam giving effects such as large scattering, beam deflection and increased noise. The noise caused by the material structure is modelled as a separate layer which is super -positioned on top of the defect response simulation, meaning that the defect response is not affected by the noise. If a noise simulation is used, it must be used together with additional attenuation modeling as mentioned above or else the result will be a non -conservative signal to noise ratio for any give indication. [11]

9. CIVA 11 Applications in the Evaluation of the Ultrasonic Standards

9.1. Determination of the FBH's ultrasonic responses

The goal of this virtual determination is to measure the difference [dB] between the signals obtained from Flat Bottom Holes of different diameters positioned at the same depth into the examined material. The obtained values will be compared with the theoretical difference calculated according to the Kirchhoff Approximation.

The scanning of three references blocks with the followings dimensions is performed:

- Flat faced reference block, 111 x 111 mm square dimension,
- Round reference block, 111 mm diameter,
- Round reference block, 265 mm diameter.

Each reference block is provided with one pair of FBH having the diameters of Φ1.2 and Φ 2.0 mm for the first determination and Φ 0.8 mm and Φ1.2 mm for the second determination. All holes are positioned with the flat surface at 50 mm below the entry surface of the ultrasonic beam.
The ultrasonic transducers used for these simulations are the following:
STS 20 P5 – immersion transducer, non-focused, 20 mm crystal diameter, 5MHz central frequency.
STS 20 P5 L125 – immersion transducer, 125 mm focal distance in water, 20 mm crystal diameter, 5MHz central frequency.
STS 20 P5 L200 - immersion transducer, 200 mm focal distance in water, 20 mm crystal diameter, 5MHz central frequency.
Sound path in water is set 100 mm for all cases. Sound speed in material and specific attenuation are identical for all determinations (see Figure 22, Figure 23 and Figure 24).
The left side figure presents the echo-dynamic registration of the echoes obtained by scanning each of the two FBH. In the same time, the amplitude of the echoes and difference between signals from the holes can be direct read.
The right side figure represents the examination technique related to the reference block used and the holes positions.

Preprints (www.preprints.org) | NOT PEER-REVIEWED | Posted: 9 May 2019 doi:10.20944/preprints201905.0111.v1

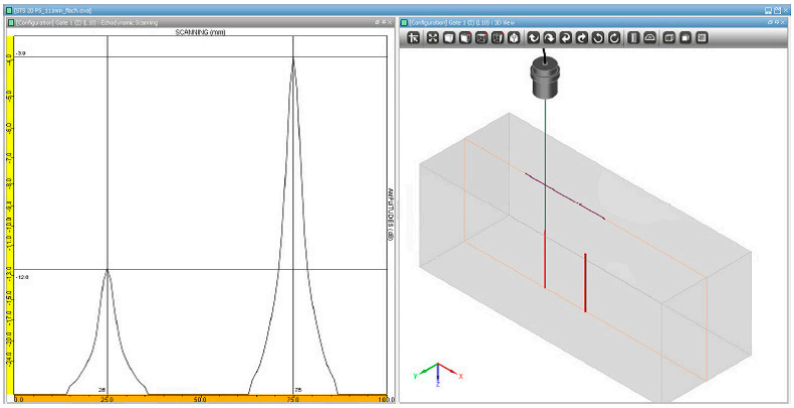

Figure 22. Scanning of the flat-faced 111x111 mm billet

Each reference block was scanned successively with each of the three transducers, respectively 18 measurement for the pair Φ 2.0-Φ 1.2 mm FBH and similarly for the pair Φ 1.2 - Φ 0.8 mm FBH. The results of the test are presented in Table 2 and Table 3 (see below).

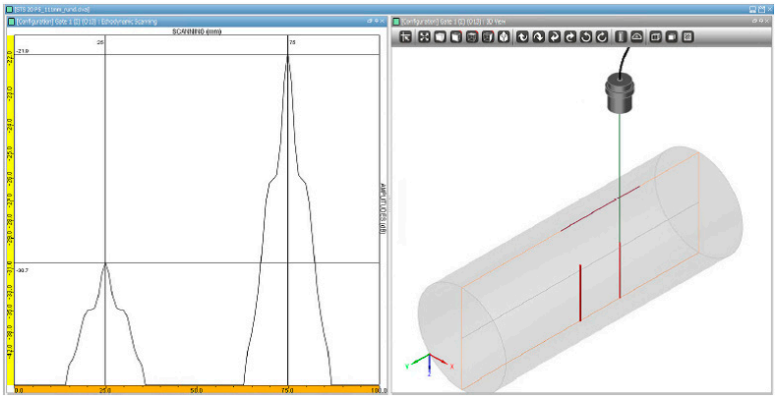

Figure 23. Scanning of the Φ 111 mm billet

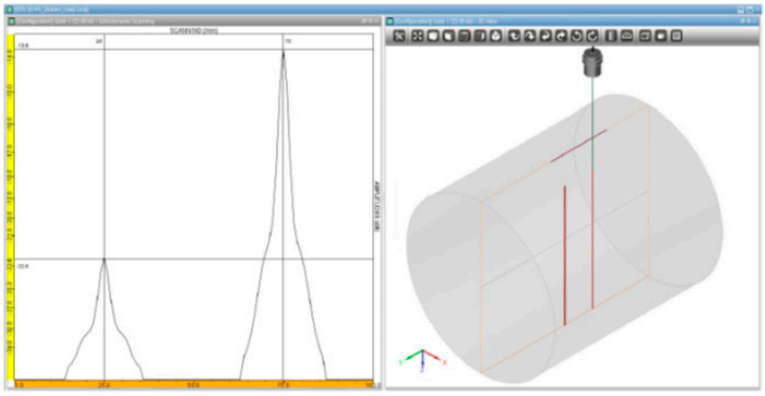

Figure 24. Scanning of the Φ 265 mm billet

10. Results

10.1. Comparison between Signals

We observe that, for the FBH pair of Φ 1.2 - Φ 2.0 mm, the amplitude differences obtained with CIVA 11 are in the range of 8.6÷8.8 dB, very close of the theoretical value of 8.87 dB (see Table 2). Similarly, for the FBH pair of Φ 0.8-Φ 1.2 mm, the differences determined by the program are in the range of 6.8÷7.0 dB and the calculated value is 7.04 dB (see Table 3).

Preprints (www.preprints.org) | NOT PEER-REVIEWED | Posted: 9 May 2019 doi:10.20944/preprints201905.0111.v1

The resulting values (noted with Δ in Table 2 and Table 3) match the theoretical values obtained for the proportion of the surfaces of the artificial defects. For defects smaller than the wavelength, it was proven in reality that the differences between the two holes are different that these values (please refer to Figure 16). As observed, these differences are more pronounced as the product *ka* >>1 (k=wave number and a=size of the artificial defect).

Table 2- Comparison of difference between Signals of FBHs Φ 1.2 and Φ 2.0 mm

Test specimen	Test flaw	STS 20 P5		STS 20 P5 L125		STS 20 P5 L200	
billet 111x111 mm	FBH Ø 1.2 mm	-12.6 dB	Δ=8.7 dB	-9.4 dB	Δ=8.7 dB	-8.6 dB	Δ=8.6 dB
	FBH Ø 2.0 mm	-3.9 dB		-0.7 dB		0 dB	
Bar Ø 111 mm	FBH Ø 1.2 mm	-30.7 dB	Δ=8.8 dB	-16.8 dB	Δ=8.8 dB	-21.3 dB	Δ=8.7 dB
	FBH Ø 2.0 mm	-21.9 dB		-8 dB		-12.6 dB	
Bar Ø 265 mm	FBH Ø 1.2 mm	-22.6 dB	Δ=8.8 dB	-11.6 dB	Δ=8.7 dB	-14.1 dB	Δ=8.7 dB
	FBH Ø 2.0 mm	-13.8 dB		-2.9 dB		-5.4 dB	

Table 3- Comparison of difference between Signals of FBHs Φ 0.8 and Φ 1.2 mm

Test specimen	Test flaw	TS 20 WB4		STS 20 P5 L125		STS 20 P5 L200	
billet 111x111 mm	FBH Ø 0.8 mm	-7.2 dB	Δ= 7 dB	-7.7 dB	Δ= 7 dB	-6.9 dB	Δ= 6.9 dB
	FBH Ø 1.2 mm	-0.2 dB		-0.7 dB		0 dB	
Bar Ø 111 mm	FBH Ø 0.8 mm	-21.9 dB	Δ= 7 dB	-15.2 dB	Δ= 7 dB	-19.7 dB	Δ= 7 dB
	FBH Ø 1.2 mm	-14.9 dB		-8.2 dB		-12.7 dB	
Bar Ø 265 mm	FBH Ø 0.8 mm	-14.5 dB	Δ= 6.8 dB	-9.9 dB	Δ= 6.9 dB	-12.3 dB	Δ= 6.8 dB
	FBH Ø 1.2 mm	-7.7 dB		-3 dB		-5.5 dB	

These experiments prove the limitations of the CIVA 11 simulation software for the defects close to the specular area and geometrical reflex whereas the software applies the Kirchhoff Approximation and does not consider the diffraction phenomenon that appear at the edge of FBH (see Chap. 7).

10.2. Optimization of the Ultrasonic Inspection

The simulation software can also be used for the selection of the main features of the ultrasonic transducers in relation with the examination technique for the inspection of the immersed plates and forged bars.

Table 2 and Table 3 also provide the data relevant for the efficiency of each type of transducer at a certain depth for a specific radius of the entry surface.

The transducer with the best ultrasonic behavior for this scenario can be decided by comparing the observed amplification reserve with the value initially selected for each of the 3 transducers.

For an example, if Table 2, row 1 - billet 111x111 mm and Table 2, row 2 - BAR Φ111 mm are selected:

Row 1, FBH Φ 1.2 mm represents the inspection of a defect located at a depth of 50 mm below the entry plane surface. The best result is provided by the transducer STS 20 P5 L 200 (-8,6 dB) due to optimal Pulse Volume for a defect located at a 50 mm depth related to its focal distance in water

and the entry plane surface. The gain differences comparing with the other transducers are relatively small: 0.8 dB versus STS 20 P5 L 125 and 3.0 dB versus STS 20 P5 (unfocused).
The situation is significantly different when the Φ 111 mm billet is inspected.
The most efficient transducer is STS 20 P5 L 125 with a focal length in water of 125 mm. Due to the radius of the entry surface, the focal distance in the material is increased (see para 6.) and this transducer presents now the focal distance in the area of depth of the artificial defect (50mm). The gain difference is increased significantly comparing with the other 2 transducers: 4.5 dB versus the transducer focalized with the focal distance of 125 mm and 13.9 dB versus the unfocalized transducer. This is caused by the defocusing of the immersion transducers at incidence of the ultrasonic beam with the cylindrical surface of the billet and due to the modification of the Pulse Volume in the area of the targeted defect.

11. Conclusion

The accurate prediction of absolute noise levels requires detailed knowledge of the metal microstructure which enters the model calculations through certain frequency-dependent factors known as "backscatter coefficients" or "Figures-of-Merit". For a typical industrial inspection of a billet or forging, such FOM information is not generally available, although it could be deduced by analyzing backscattered noise waveforms from regions where the microstructure is spatially uniform. In the absence of specific FOM information it is still possible to use the noise models in a productive manner, namely to predict how changes in the inspection procedure or component geometry will affect the backscattered noise from some microstructure at hand. The analysis of the noise of the material requires the analysis of the physical detection possibilities in relation with the material's dimensions.
The inspection's optimization is achieved both by minimizing the noise of the material and by adopting the inspection techniques capable to highlight and perform a correct evaluation of the discontinuities smaller than one wavelength.
Unfortunately, the largest discrepancy between the software simulations and experiments is noise or rather signal to noise ratio. Defects responses are often evaluated in relation to the surrounding noise levels rather than an arbitrary reference target, such as FBH.
The issues described above clearly indicate that it is not possible to simulate a complete inspection, or validate an inspection procedure by simulations with CIVA at the current time. The conclusion is that simulations using CIVA can be used when specific problems or technical solutions must be solved or developed, e.g. the influence of the surface curvature over the Pulse Volume or the correct choice of the inspection equipment.

Acknowledgement

This work was supported by S.C. ZIROM-S.A – Giurgiu - ROMANIA and was performed by the NDT Consulting Company - DIAC SERVICII srl.

References

1. Sharfine Shahjahan, Pierre-Emile Chillier, Bertrand Chassignole –" Etude expérimentale de l'influence de la microstructure sur la détection de défauts plans"- EDF – CEIDRE, EDF LAB - Site des Renardières- Journees Cofrend 2017
2. F. J. Margetan, Kim Y. Han, I. Yalda, Scot Goettsch and R.B Thompson, "The practical application of grain noise models in titanium billet and forgings", Review of Progress in QNDE, Vol. 14B, eds. D.O. Thompson and D.E. Chimenti (Plenum, New York, 1995)
3. Anton Van Pamel. – Ultrasonic Inspection of Highly Scattering Materials- Imperial College London - Department of Mechanical Engineering- October 2015
4. Linxiao Yu.- Understanding and improving ultrasonic inspection of jet-engine titanium alloy – Iowa State University 2004
5. Margetan, F.J.1, Umbach, J.2, Roberts, R.1, Friedl, J.1, Degtyar. - Inspection

 doi:10.20944/preprints201905.0111.v1

Development for Titanium Forgings - *DOT/FAA/AR-05/46* - Air Traffic Organization Operations Planning Office of Aviation Research and Development Washington, DC 20591 May 2007

6. F. J. Margetan, I. Yalda and R. B. Thompson. – Ultrasonic Grain Noise Modeling: Recent Applications to Engine Titanim Inspections - Review of Progress in Quantitative Nondestructive Evaluation, Vol. 16- Edited by D.O. Thompson and D.E. Chimenti, Plenum Press, New York, 1997
7. Wolfram A. Karl Deutsch, Michael Joswig. - Automated Ultrasonic Testing – Systems for Bars and Tubes - 11th European Conference on Non-Destructive Testing (ECNDT 2014), October 6-10, 2014, Prague, Czech Republic
8. BA Auld – "Acoustic fields and waves in solids" vol. ii, 1990.
9. J. Krautkrämer: "Fehlergrößenermittlung mit Ultraschall", Archiv für Eisenhüttenwesen 30, pp. 693-703, 1959.
10. M. Darmon, V. Dorval, A. Kamta Djakou. - A system model for ultrasonic NDT based on the Physical Theory of Diffraction (PTD)
11. Gustav Holmer, Will Daniels, Tommy Zettervall – "Evaluation of the simulation software CIVA for qualification purpose" - Swedish Radiation Safety Authority